

Aqueous Magnesium-Ion Battery Anode with 75,000 Cycles Lifespan

Yu Wu,[§] Shunning Li,[§] Bowen Jin,^{*} Yusen Yang, Jiahui Zeng, Mingfei Shao,^{*} Feng Pan,^{*} and Xue Duan



Cite This: <https://doi.org/10.1021/jacs.5c21656>



Read Online

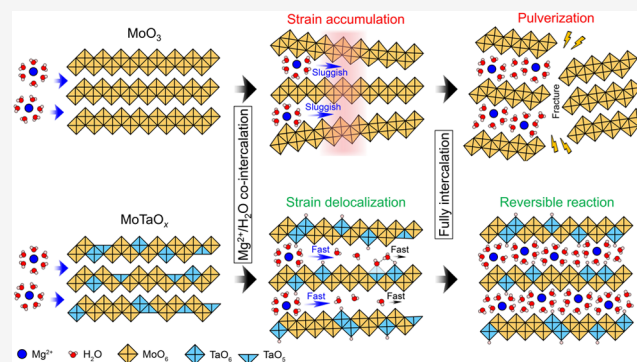
ACCESS |

Metrics & More

Article Recommendations

Supporting Information

ABSTRACT: Aqueous magnesium-ion batteries (AMIBs) are garnering growing interest due to their abundant resources, inherent safety, and low cost. However, the strong Mg^{2+} - H_2O interaction results in bulky hydrated metal ions that diffuse sluggishly within host materials, leading to structural degradation and poor cycling performance. Here, we report a strain delocalization strategy to preserve structural robustness and achieve ultrastable cycling stability of AMIBs by using self-ordered Ta-doped MoO_3 (MoTaO_x) nanotube array electrodes. Oxygen vacancies within MoTaO_x can facilitate the accommodation and dissociation of interlayer H_2O molecules, leading to the formation of a Ta-OH...OH₂ configuration. This reduces the kinetic energy barrier for Mg^{2+} diffusion, resulting in the uniform magnesiation of MoTaO_x , where the rigid Ta-O bonds further enable delocalization of mechanical strain throughout the host, conferring a shear strain tolerance of $\sim 95\%$ during magnesiation. The MoTaO_x electrode exhibits stable operation over 75,000 cycles and delivers a cumulative capacity of 7.2 kAh g^{-1} , significantly surpassing previous reports. These findings elucidate the sluggish H_2O co-intercalation-induced localized strain as a degradation pathway and establish vacancy-pinned, water-regulated magnesiation for delocalization of strain as a viable design principle for developing long-lifespan AMIBs with high capacity.



INTRODUCTION

The intensification of global energy demand has driven the advancement of high-performance, cost-effective, and sustainable energy storage technologies. Among various energy storage systems, magnesium-ion batteries have attracted considerable attention due to their nontoxicity and high volumetric energy density. In particular, eco-friendly aqueous magnesium-ion batteries (AMIBs), due to the widespread availability of magnesium resources ($\sim 2.9 \text{ wt } \%$ in the earth's crust), safety, and low-cost water-based electrolytes, offer a compelling alternative to mitigate safety risks and reduce both material and manufacturing costs.^{1–8} Moreover, Mg^{2+} ions possess relatively small ionic radii (0.72 \AA),⁹ which theoretically facilitates the intercalation into host materials with a limited expansion of the lattice. In this context, AMIBs emerge as promising candidates for deployment in large-scale energy storage systems and other applications, where stringent safety standards are imperative. Despite their inherent safety and cost advantages, AMIBs face significant challenges that impede their commercial viability. For example, their limited cycle lifespan increases the maintenance demands and operational costs. Furthermore, the practical energy densities achieved are substantially lower than theoretical predictions, restricting their use in high-energy-demand applications.¹⁰ These limitations underscore the need for continuous research to enhance the performance and commercial prospects of the AMIB technologies.

To achieve long cycle life and high energy density in AMIBs, it is critical to develop Mg^{2+} ion storage electrodes that combine outstanding stability with high capacity. To date, a diverse range of materials have been explored for Mg^{2+} storage, including organic compounds (e.g., polyimide, perylene diimide), Chevrel-phase compounds (Mo_6S_8), manganates, and transition metal oxides (e.g., MnO_2 , V_2O_5 , MoO_3).^{11–17} Among these, transition metal oxides have emerged as especially promising due to their high theoretical capacity (e.g., $\text{MoO}_3 > 300 \text{ mAh g}^{-1}$). Although this exceptional energy density has stimulated considerable research interest, electrochemical decay during divalent Mg^{2+} (de)intercalation leads to poor cycling stability—a critical factor for practical applications.^{18,19} This can be ascribed to the strong electrostatic interaction between divalent Mg^{2+} and solvent molecules (H_2O), which forms a tight Mg^{2+} -OH₂ coordination (Mg-O as short as 2.04 \AA) and a high desolvation enthalpy.²⁰ Consequently, Mg^{2+} often migrates as a coordinated hydrated species (e.g., $[\text{Mg}\cdot 6\text{H}_2\text{O}]^{2+}$) and undergoes ion/solvent co-intercalation, which can enlarge the host lattice and induce

Received: December 4, 2025

Revised: February 7, 2026

Accepted: February 11, 2026

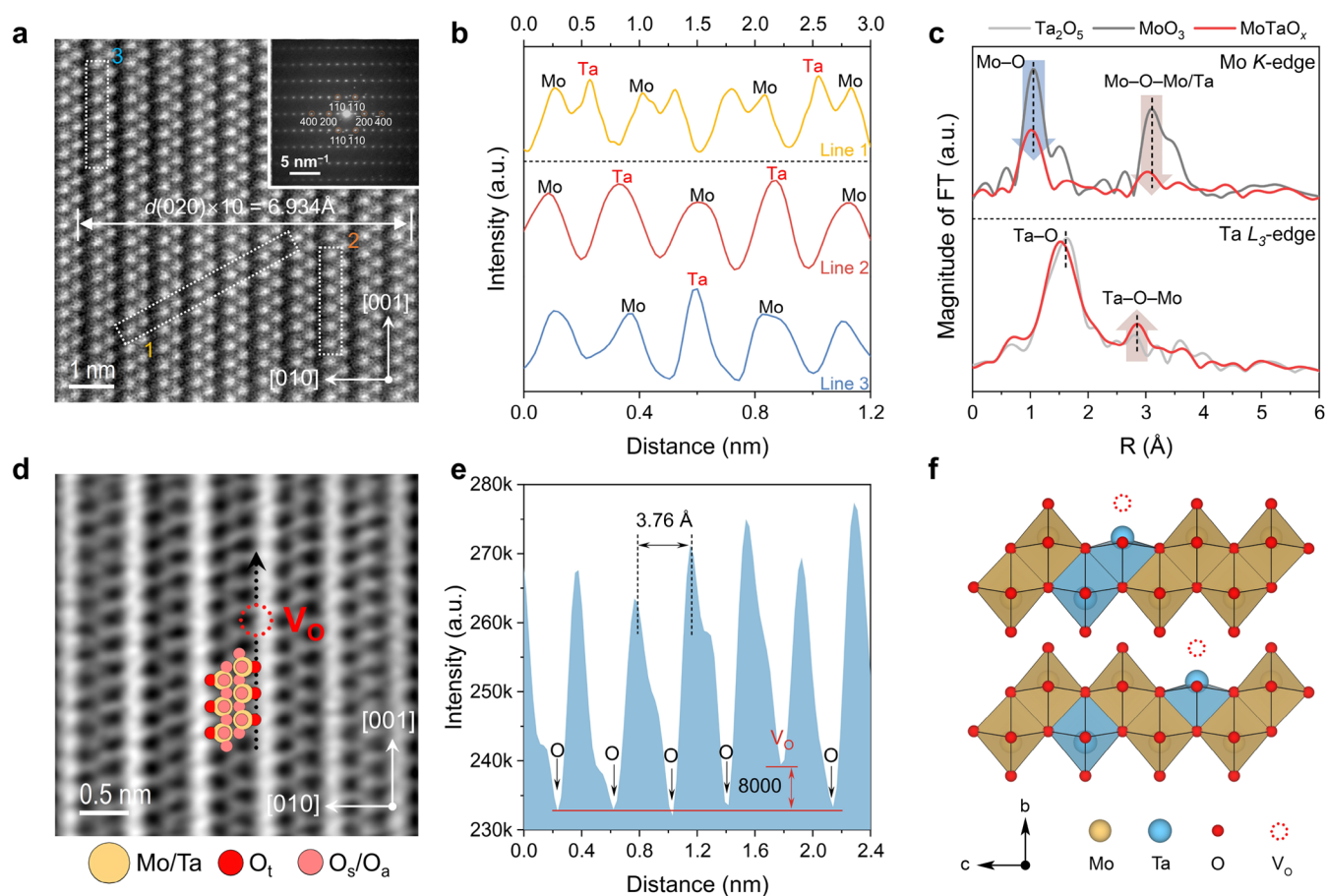


Figure 1. Structure characterizations of MoTaO_x. (a) STEM image of MoTaO_x with corresponding SAED patterns inset. (b) Intensity profiles corresponding to labeled lines in (a). Fourier-transformed EXAFS spectra of the (c) Mo K-edge and Ta L₃-edge. (d) ABF-STEM image of MoTaO_x. (e) Intensity profile corresponding to the black dashed line in (d), as directed by the arrow. (f) Schematic model of MoTaO_x.

substantial strain.^{21–24} Meanwhile, the strong interaction between Mg²⁺ and the host lattice further aggravates sluggish ion transport and triggers irreversible structural degradation (e.g., pulverization), collectively limiting Mg²⁺ storage capability and compromising both cycling stability and overall energy/power output.^{10,12,25} These structural cracking and pulverization are usually induced by anisotropic lattice (localized) strain yielded on insertion chemistry, especially about multivalent ions (e.g., Mg²⁺). Therefore, to date, effective strain mitigation enabling long-term cycling stability for Mg²⁺-storage electrodes has not been achieved and remains a major challenge.

Here, we demonstrate a strain delocalization strategy by using a self-ordered Ta-doped MoO₃ (MoTaO_x) nanotube array electrode for ultralong operation in AMIBs. MoTaO_x preserves the orthorhombic structure of MoO₃ while introducing oxygen vacancies (V_O) at terminal oxygen sites adjacent to the Ta dopants. These V_O are utilized to accommodate and dissociate interlayer H₂O molecules to form “Ta–OH...OH₂” species, significantly lowering the kinetic energy barrier for bulky hydrated Mg²⁺ diffusion. By this process, the accumulation of localized internal strain—arising from steep concentration gradients and pronounced interlayer expansion in magnesiated regions caused by Mg²⁺/H₂O molecules co-intercalation (e.g., ~11H₂O per Mg²⁺ in MoO₃)—is effectively mitigated. As a result, a high capacity of 300 mAh g⁻¹ at 0.15 A g⁻¹ and the ultrastable cyclability over 75,000 cycles were achieved in the MoTaO_x electrode,

delivering a maximum cumulative capacity of 7.2 kWh g⁻¹, which is 7.2 times higher than the best value reported to date.

RESULTS AND DISCUSSION

Structure and Composition Analysis

The Ta-doped MoO₃ nanotube array sample (MoTaO_x) was synthesized via a straightforward anodization and annealing process (Figure S1). As depicted in Figure S2a, vertically self-ordered nanotubes with a length of 1.2 μm and an inner diameter of 125 nm were successfully fabricated, establishing electrical connectivity with the MoTa alloy current collector. Energy dispersive X-ray (EDX) mapping of MoTaO_x (Figure S2b) revealed a homogeneous distribution of Mo, Ta, and O elements throughout the nanotubes, confirming the successful incorporation of Ta into the MoO₃ matrix. X-ray diffraction (XRD) patterns and Rietveld refinements of MoTaO_x indicated an orthorhombic *Pbnm* symmetry identical to that of pristine MoO₃ (JCPDS No. 05–0508),²⁶ with lattice parameters of *a* = 3.962 Å, *b* = 13.867 Å, and *c* = 3.698 Å (Figure S2c). This suggests that Ta substitutes the Mo atoms in the lattice, maintaining the orthorhombic structure of MoO₃ with an approximate Ta weight fraction of 30 wt %. Moreover, the minor changes in lattice parameters, particularly the slight increase in the *b*-spacing (Tables S1 and S2), corroborate the introduction of larger Ta atoms into the Mo sites. Aberration-corrected scanning transmission electron microscopy (STEM) was further employed to directly visualize the lattice

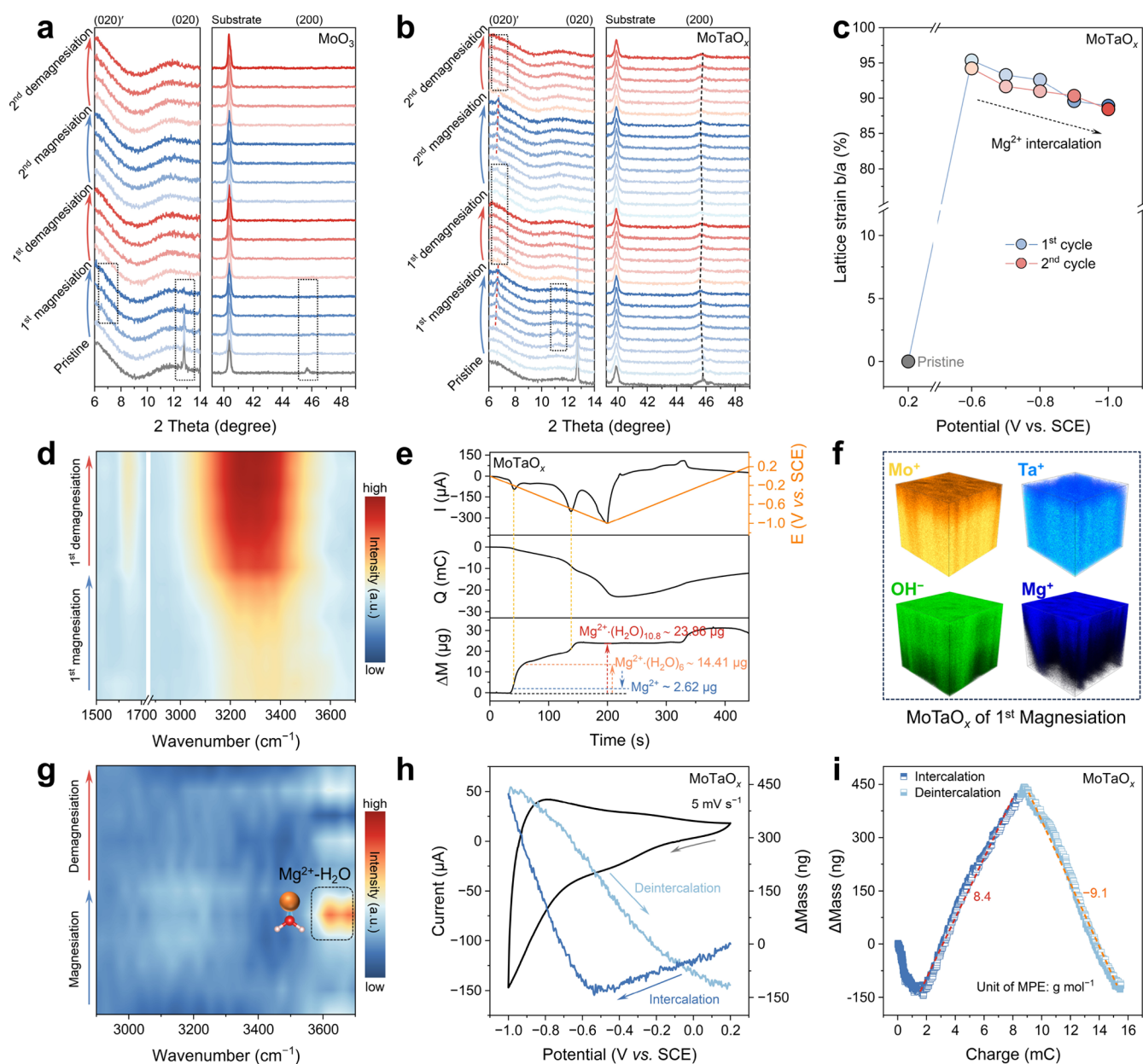


Figure 2. Probing hydrated Mg^{2+} and free H_2O cointercalated in interlayers of MoO_3 and MoTaO_x . *Operando* XRD of (a) MoO_3 , and (b) MoTaO_x in the initial two cycles. (c) Shear strain changes during the first and second magnesiaion process, (d) *operando* ATR-FTIR spectra, and (e) electrode mass change during the first magnesiaion of MoTaO_x . (f) Depth profiling of the Mo^+ , Ta^+ , Mg^+ , and OH^- secondary-ion fragments in magnesiaion MoTaO_x acquired by TOF-SIMS. (g) *Operando* ATR-FTIR differential spectra, (h) electrode mass change, and (i) $\Delta\text{M}-\Delta\text{Q}$ curve during a stable cycle of MoTaO_x .

parameters and the distribution of Ta species. As shown in Figures 1a and S3a,d, MoTaO_x exhibits a typical layered structure with an interlayer distance of 6.934 Å. The intensity profiles along the zone axis (Figures 1b and S3b and e) confirmed that the bright spots corresponding to Ta atoms precisely occupy the lattice sites of Mo atoms in MoO_3 . The chemical valence states of MoTaO_x were investigated by using X-ray photoelectron spectroscopy (XPS). The high-resolution XPS spectra for Mo (Figure S4a) showed spin-orbit split peaks at 236.2 and 233.05 eV, consistent with Mo^{6+} , indicating a high oxidation state of Mo in MoTaO_x .^{26,27} Similarly, the XPS spectra for Ta (Figure S4b) displayed a binding energy of Ta 4f 5/4 and Ta 4f 7/4 at 28.3 and 26.4 eV, respectively, corresponding exclusively to Ta^{5+} in the nanotubes.²⁸

To elucidate the electronic structure and local coordination environment of Mo and Ta atoms in MoTaO_x , X-ray absorption near-edge structure (XANES) and extended X-ray absorption fine structure (EXAFS) spectroscopies were conducted. Both Mo and Ta species in MoTaO_x (Figure S5a, b) exhibited spectral shapes similar to their high-valence oxide references (MoO_3 and Ta_2O_5 , respectively). The Fourier-transformed EXAFS spectra of the Mo K-edge (Figure 1c) revealed two prominent peaks at approximately 1.01 Å and 3.04 Å, corresponding to the first Mo–O shell contribution and the second Mo–O–Mo/Ta contribution, respectively.²⁹ The intensities of Mo–O and Mo–O–Mo peaks for MoTaO_x are significantly lower than those for MoO_3 , indicating that the average coordination numbers of Mo–O

and Mo–O–Mo in MoTaO_x are well below those in MoO₃.^{30,31} And the structure with low coordination numbers results in shortening of the Mo–O–Mo bond length in MoTaO_x. The Fourier-transformed EXAFS spectra of the Ta L₃-edge displayed peaks indicative of the first Ta–O shell contribution and the second Ta–O–Ta shell contribution at around 1.53 Å and 2.85 Å, respectively.^{28,32} But the intensities of Ta–O–Ta peaks for MoTaO_x are higher than those for Ta₂O₅, indicating that the average coordination numbers of Ta–O–Ta in MoTaO_x exceed those in Ta₂O₅.^{30,31} Hence, these findings confirm the successful incorporation of Ta atoms into the MoO₃ lattice with relatively compact bonding. Some of Mo atoms in MoO₃ are replaced by Ta atoms, and due to charge compensation (the valence of Ta⁵⁺ is lower than Mo⁶⁺), oxygen vacancies (V_O) are introduced at the terminal oxygen sites (O_v, singly coordinated to the Mo) in MoTaO_x, which are detected by angular bright-field aberration-corrected scanning transmission electron microscopy (ABF-STEM) (Figures 1d, e, S6 and Supporting Note S1). This result can be further supported by density functional theory (DFT) calculations (Figure S7) that indicate the thermodynamic preference of V_O forming at the terminal oxygen sites of MoTaO_x and in the vicinity of Ta atoms. Figure 1f shows the schematic model of MoTaO_x. All characterization results substantiate the coherent growth of MoTaO_x, confirming the successful structural and material design.

For comparison, pure MoO₃ nanotubes were fabricated by using the same method on a Mo foil substrate. Scanning electron microscopy (SEM) images (Figure S8) showed that the MoO₃ nanotubes exhibited a similar thickness and diameter to MoTaO_x, with vertical alignment on the Mo substrate. The lattice-resolved STEM image of the pure MoO₃ nanotubes displayed a *d*-spacing of 0.693 Å, corresponding to the (020) planes of α-MoO₃ (Figure S9), which is slightly shorter than that of MoTaO_x. This observation is consistent with the XRD patterns and Rietveld refinement results (Figure S10, Tables S1 and S2, JCPDS No. 05–0508).²⁶ Raman spectroscopy of MoTaO_x and MoO₃ (Figure S12) revealed several analogous peaks in the range of 100–1100 cm⁻¹, corresponding to in-plane and bending vibration modes of Mo–O bonds,³³ indicating that the coordination environments of Mo in MoTaO_x are similar to those in pure MoO₃.

Co-Intercalation of Mg²⁺ and H₂O

To investigate the intercalation processes of MoO₃ and MoTaO_x in situ X-ray diffraction (XRD) experiments were conducted during the initial two complete (de)magnesiumation cycles (Figure 2a,b). Pristine MoO₃ exhibited a layered structure along the *b*-axis, with a diffraction peak at 2θ = 12.76°, corresponding to the (020) plane. During the intercalation process, the intensity of the peak at 2θ = 45.74° (corresponding to the (200) plane) decreased as the applied potential was decreased. Concurrently, upon charging at –0.4 V versus saturated calomel electrode (SCE), a new peak emerged at 2θ = 6.53°, designated as (020)'. The lattice parameter along the *b*-axis was plotted as a function of intercalation (Figure 2c), revealing an unexpected 95% expansion in the *b*-axis lattice parameter during the intercalation process. This substantial expansion resulted in an ultralarge volume variation of 95% and significant strain evolution. Unfortunately, at the fully magnesiated state, all diffraction peaks corresponding to the (020), (020)', and (200) planes disappeared, suggesting electrode pulverization

due to extreme volume variation. As shown in Figure S13 and Supporting Note S2, the detached fragments were meticulously collected and examined by XRD. The diffractogram reveals the coexistence of reflections from two expanded interlayer spacings (11.7 Å and 7.2 Å) together with the pristine layers (6.9 Å), indicating substantial interlayer spacing mismatch caused by a huge concentration gradient between the magnesiated region and nonmagnesiated region during magnesiation with sluggish Mg²⁺ migration. This severe volumetric mismatch induces accumulation of pronounced, localized internal strain, ultimately leading to cracks and pulverization of MoO₃. Optical and SEM images further corroborate these findings, showing that the activation material was pulverized and partially detached from the current collector after the initial intercalation process (Figure S14). In situ electrochemical quartz crystal microbalance (EQCM) measurements were employed to monitor the mass changes of the electrode, thereby elucidating the intercalation and pulverization processes. As illustrated in Figure S15, a mass increase was detected upon application of a potential of –0.1 V (indicated by the first peak highlighted with a yellow dashed line), corresponding to the intercalation of hydrated Mg²⁺ ions. Subsequently, a severe mass loss was observed during the intercalation process, attributable to electrode pulverization.

In contrast to MoO₃, the structural evolution of MoTaO_x exhibits high reversibility (Figure 2b). During the intercalation process at a potential of –0.6 V vs SCE, the diffraction peak at 2θ = 12.76° gradually diminishes, while new peaks emerge at 2θ = 11.22° and 6.51°. As the applied potential decreases to –0.8 V vs SCE, the peak at 2θ = 11.22° disappears, and the peak at 2θ = 6.51° shifts to 2θ = 6.72°, indicating lattice contraction along the *b*-axis during the intercalation process, which is attributed to electrostatic interaction between the embedded Mg²⁺ ions and lattice layers. Conversely, the lattice parameter along the *a*-axis ((200) plane) remains nearly constant until the completion of intercalation. Moreover, unlike MoO₃, the fully magnesiated MoTaO_x does not exhibit multiple (020)' reflections, indicating a coherent interlayer response and effective delocalization of strain induced by Mg²⁺ insertion. During the subsequent deintercalation process, the (020)' peak disappears, suggesting lattice distortions at different locations. In the following cycle, the characteristic features of the (020)' plane in MoTaO_x reversibly emerge, shift, and disappear, demonstrating the structural stability of the gallery framework structure during cycling. Further analysis of the lattice parameters and volumetric variations during the intercalation process reveals shear strains of approximately 95% and 89% at the onset and the end of magnesiation in MoTaO_x, respectively (Figure 2c; calculation details are in Supporting Information). Notably, the substantial lattice expansion along the *b*-axis is unlikely attributable to the intercalation of bare Mg²⁺ ions, as MoTaO_x exhibits significantly lower lattice expansion in an organic electrolyte (Figure S16 and Supporting Note S3). Nonetheless, the specific species intercalated into the MoTaO_x lattice remains to be elucidated.

In aqueous electrolytes, six H₂O molecules coordinate efficiently with the central Mg²⁺ ion, forming the solvation structure Mg·(H₂O)₆, which is likely related to the significant lattice expansion observed. To investigate this phenomenon, *operando* attenuated total reflectance Fourier transform infrared (ATR-FTIR) spectroscopy was performed. An increase in the O–H bending mode and stretching mode signals of H₂O, observed at approximately 1630 cm⁻¹ and

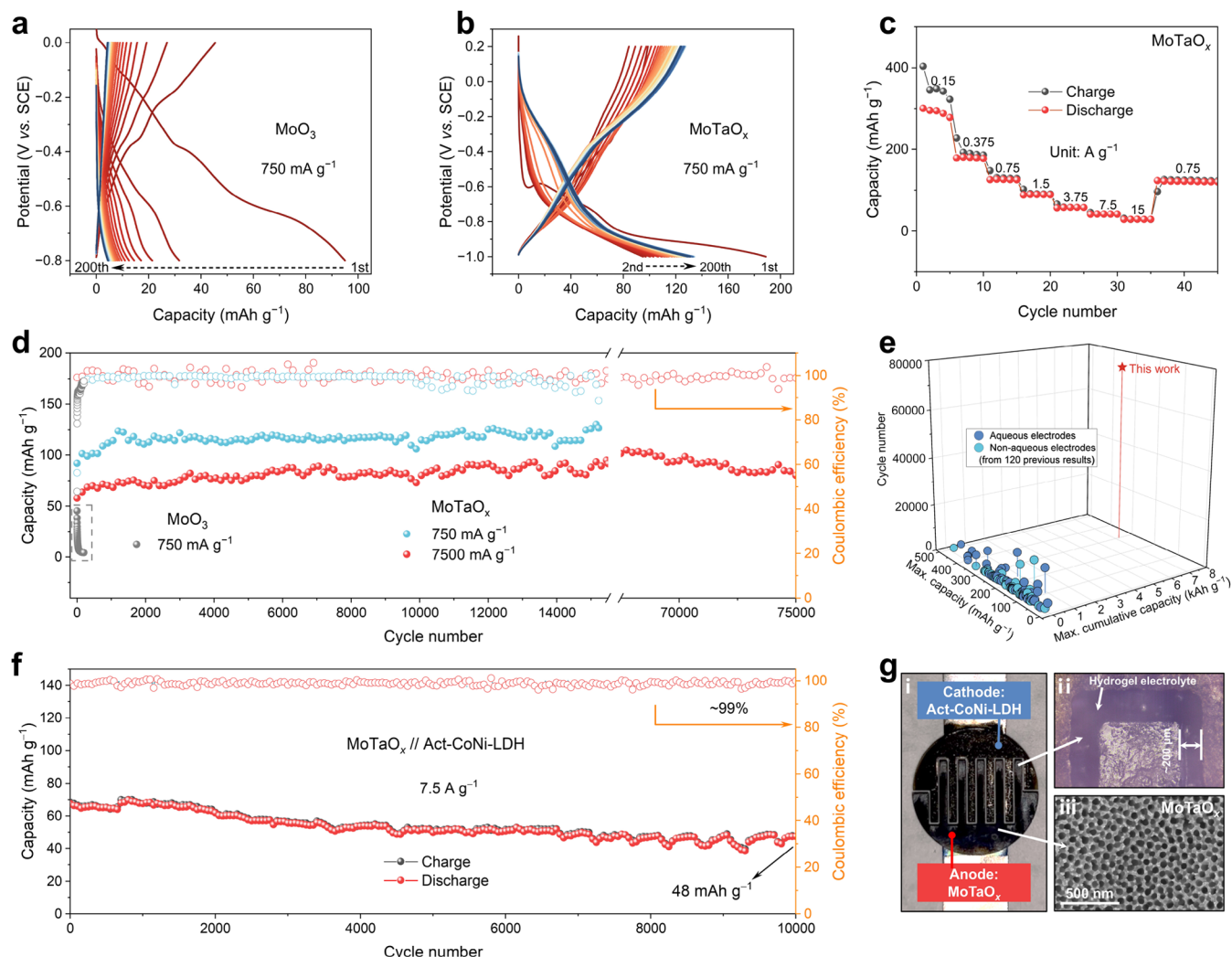


Figure 3. Electrochemical behavior of the MoTaO_x electrode. Galvanostatic charge/discharge profiles of (a) MoO_3 and (b) MoTaO_x from 1st to 200th cycles at 750 mA g^{-1} . (c) Rate capability of MoTaO_x . (d) Cycling performance comparison of MoO_3 and MoTaO_x at 750 and 7500 mA g^{-1} . (e) Electrochemical performance (maximum capacity, maximum cumulative capacity, and cycling life) of the MoTaO_x electrode and representative electrode materials in MIBs. (f) Cycling performance of assembled Act-CoNi-LDH// MoTaO_x aqueous magnesium-ion full cell. (g) Assembled Act-CoNi-LDH// MoTaO_x interdigital micro-AMIB. (i) Photographs of Act-CoNi-LDH and MoTaO_x electrode, (ii) optical microscope image for local magnified view of channel, and (iii) SEM image of interdigital MoTaO_x electrode.

$3200\text{--}3400 \text{ cm}^{-1}$, respectively, was detected during the initial magnesiation process, indicating the intercalation of solvated Mg^{2+} ions into the MoTaO_x lattice.³⁴ Interestingly, the intensity of the H_2O peaks continued to rise during the initial demagnesiation process, suggesting that additional H_2O molecules are intercalated into the MoTaO_x lattice during demagnesiation (Figure 2d).

To quantify the number of H_2O molecules electrochemically cointercalated into the MoTaO_x interspace, mass changes during the initial cycle were measured by EQCM. Figure 2e illustrates two mass mutation points observed at current increase events corresponding to potentials of -0.2 V and -0.8 V (indicated by yellow dashed lines). Molar weights calculated from the electrode mass change versus charge ($\Delta M\text{-}\Delta Q$) plots indicate the intercalation of Mg^{2+} ions with high hydration levels. The number of cointercalated H_2O molecules for each Mg^{2+} was determined to be as high as 10.8, suggesting that the intercalation of Mg^{2+} ions could not only bring along the H_2O molecules in their first solvation sheath but also facilitate the entry of free H_2O molecules that are not coordinated with

Mg^{2+} . During the demagnesiation process, the mass continues to increase even as the charge is depleted, indicating that the expulsion of hydrated Mg^{2+} ions from the interlayer is accompanied by the intercalation of additional H_2O molecules, which is consistent with the *operando* ATR-FTIR results. Furthermore, the architectures of intercalated Mg^{2+} and H_2O are visualized in Figure 2f, which depicts a 3D distribution of Mg-related and OH-related fragment ions. In the magnesiation state, the cointercalated Mg^{2+} and H_2O molecules are homogeneously distributed within the bulk of MoTaO_x . Notably, no molybdenum bronze phase was detected, indicating negligible H^+ intercalation, which is consistent with the negligible pH change of MoTaO_x surface in 1 M MgSO_4 during cycling and the small lattice expansion of hydrogenation MoTaO_x (Figure S17, Supporting Note S4, and Table S3). Energy dispersive X-ray spectrometry (EDS) and corresponding elemental mapping further confirm substantial Mg^{2+} intercalation (Figure S18). These findings validate that significant volume expansion and shear strain are induced by the intercalation of highly hydrated Mg^{2+} ions. Consequently,

the MoO₃ electrode undergoes structural pulverization and capacity fading, whereas the stable gallery framework of MoTaO_x is preserved following the initial cycle.

To further investigate the (de)magnesian processes in subsequent cycles, the MoTaO_x electrodes were examined in detail via *operando* ATR-FTIR differential spectra^{35,36} and EQCM measurements. The contour diagram of differential spectra revealed the presence of hydrated Mg²⁺ ions (Mg²⁺·H₂O) with weak hydrogen-bond interactions, detected at a high wavenumber of approximately 3600 cm⁻¹ during magnesian (Figure 2g). This signal is attributed to the coordination of intercalated hydrated Mg²⁺ ions with free H₂O molecules within the interlayer, forming Mg²⁺-H₂O complexes in the bulk of MoTaO_x.³⁷ Additionally, the intercalation of Mg²⁺ induces the rearrangement of H₂O molecules into a regular orientation, facilitating the formation of an ordered polyhedral structure, which is in line with XRD patterns (Figure 2b). *Ab initio* molecular dynamics (AIMD) simulations further corroborate these findings, showing that in MoO₃/MoTaO_x layers, Mg²⁺ coordinates with both interlayer water molecules and the oxide slab, exhibiting a coordination number of 4–6, with one coordination provided by a terminal oxygen atom of the MoO₃/MoTaO_x lattice (Figures S19 and S20). Notably, partially intercalated H₂O deintercalates within minutes at rest, as evidenced by a reduced interlayer spacing (Figure S21 and Supporting Note S5). After annealing MoTaO_x at 150 °C for 30 min, the spacing remains 9.8 Å, implying that a considerable fraction of interlayer H₂O persists and the robustness of the Mg²⁺-H₂O complex environment. The electrode mass changes (ΔM) associated with the Mg²⁺ (de)intercalation processes were quantified by EQCM (Figures 2h,i and S22). According to the Sauerbrey equation,³⁸ the mass change per coulomb for MoTaO_x was determined from the experimental slopes to be 8.4 g mol⁻¹ during magnesian and -9.1 g mol⁻¹ during demagnesian, both of which are lower than the value for pure Mg²⁺ (12 g mol⁻¹). This indicates topotactic intercalation and deintercalation of Mg²⁺ and H₂O within the MoTaO_x bulk, where Mg²⁺ intercalates into the electrode while expelling H₂O during magnesian, and Mg²⁺ deintercalates, accompanied by the intercalation of additional H₂O molecules during demagnesian. These findings demonstrate that the interlayer H₂O molecules introduced into the bulk of host acts as a unique, Mg²⁺-regulated spring cushion, facilitating reversible phase transitions between crystalline and amorphous states of host materials during subsequent cycling. This behavior contrasts with that of conventional layered oxide electrodes in lithium-ion batteries or sodium-ion batteries, where transition metal layers slipping typically drive the phase transition and destroy the host.^{39,40} Moreover, the MoTaO_x with water-rich interlayers provides effective electrostatic screening of the high charge density of Mg²⁺, enabling facile relaxation of the strain generated during reversible magnesian and thereby extending electrode cycling lifespan.^{13,41}

Electrochemical Performance

Electrochemical tests were conducted to evaluate the performance of MoTaO_x in comparison to MoO₃. The (dis)charge profiles of MoO₃ exhibited an initial discharge capacity of 45.4 mAh g⁻¹, which decayed to 4.3 mAh g⁻¹ after 200 cycles. In contrast, MoTaO_x demonstrated significantly enhanced capacity and cyclability, with an initial discharge capacity of 98.8 mAh g⁻¹ and a maintained capacity of 124.4 mAh g⁻¹

after 200 cycles. The slight increase in capacity is attributed to the gradual equilibrium of the inserted free water molecules. The rate capability was assessed across current densities ranging from 0.15 A g⁻¹ to 15 A g⁻¹. MoTaO_x delivered a maximum specific capacity of 300 mAh g⁻¹ at 0.15 A g⁻¹ and maintained a capacity of 28.6 mAh g⁻¹ even at a high current density of 15 A g⁻¹, highlighting its excellent rate capability (Figures 3c and S23). Notably, the reversible capacity discussed above primarily arises from the genuine (de)-intercalation of Mg²⁺ within the MoTaO_x electrode, rather than electric double-layer adsorption associated with the nanotube architecture (details in Supporting Information). As shown in Figure S24, the substrate contributed negligibly to the total capacity. Furthermore, at a mass loading of 2 mg cm⁻², both the capacity and rate performance remained stable (Figure S25). Multiple-step chronoamperometry (MUSCA) measurements and intermittent current interruption (ICI) techniques confirmed the rapid Mg²⁺ migration within the solid-state MoTaO_x (Figures S26 and S27).^{42,43} Figure 3d illustrates the long-term cycling performance of MoTaO_x at room temperature, where it maintains high capacities of 120 mAh g⁻¹ and 85 mAh g⁻¹ with remarkable approximately 100% capacity retention after 15,000 and 75,000 cycles (more than 6 month), respectively, at current densities of 0.75 A g⁻¹ and 7.5 A g⁻¹, delivering a maximum cumulative capacity of 7.2 kWh g⁻¹, which is 7.2 times higher than the best value reported to date (Figure 3e and Table S4). Additionally, the nanotube structure of MoTaO_x was preserved after cycling, indicating its high structural and electrochemical stability (Figure S28). Further electrochemical performance tests at a low current density of 0.2 A g⁻¹ corroborated the significant improvement in the cycling stability of MoTaO_x (Figure S29). The ultralong cycling life and high cumulative capacity of MoTaO_x surpass previously reported values, to the best of our knowledge.

To demonstrate the versatility of MoTaO_x, a full aqueous magnesium-ion battery was assembled using a MoTaO_x anode and an activated CoNi layered double hydroxide cathode (Act-CoNi-LDH) (Figures S30 and S31a).⁴⁴ The cyclic voltammetry (CV) curve of Act-CoNi-LDH (Figure S31b) exhibits pseudocapacitive behavior within the potential range of 0–1 V. Consequently, the assembled battery operates over a wide voltage window of 0 to 2.0 V and demonstrates rapid current response even at a scan rate of 200 mV s⁻¹. A high capacity of up to 76.6 mAh g⁻¹ is achieved at 0.375 A g⁻¹, accounting for the mass of both the anode and cathode active materials (Figure S31d). Furthermore, the full battery exhibits excellent cycling stability, maintaining a capacity of over 47.4 mAh g⁻¹ after 10,000 cycles at a current density of 7.5 A g⁻¹ (Figure 3f). Additionally, interdigital magnesium microbatteries (IMBs) were fabricated through wire-cutting and anodization processes. A digital photograph of a single IMB unit is shown in Figure 3g, with an overall size of approximately 2 cm². Optical microscopy images reveal a channel downscaling of 200 μm between the anode and the cathode within the IMB (Figure 3g). Two IMBs connected in series were able to illuminate a light-emitting diode (LED) array, demonstrating a practical application (Figure S32).

Magnesian/Demagnesian Mechanism

To elucidate the (de)magnesian mechanism, we thoroughly investigated the MoTaO_x electrodes via a series of *operando* and *ex situ* characterizations. Figure S33a presents the Mo 3d XPS profiles of the MoTaO_x electrode in pristine and

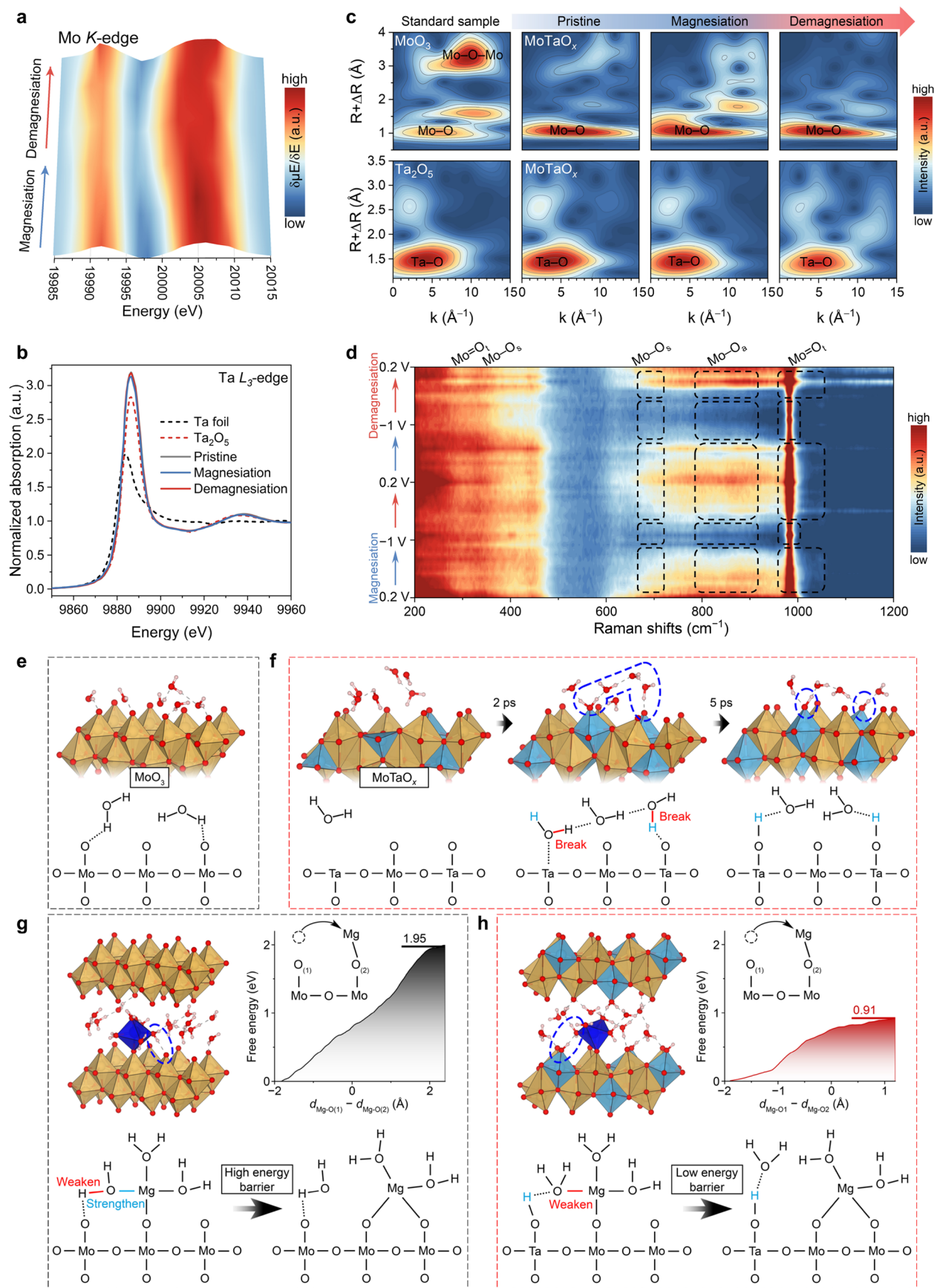


Figure 4. Energy storage mechanism study in MoTaO_x. *Operando* XANES spectra of (a) Mo K-edge as first derivative mapping and (b) Ta L₃-edge of MoTaO_x during cycling. (c) Wavelet transform (WT) of MoO₃, Ta₂O₅, and MoTaO_x in different states. (d) *Operando* Raman spectra of MoTaO_x during cycling. (e) Hydrogen bonds established between the intercalated H₂O molecules and MoO₃ slabs. (f) Dissociation of an H₂O

Figure 4. continued

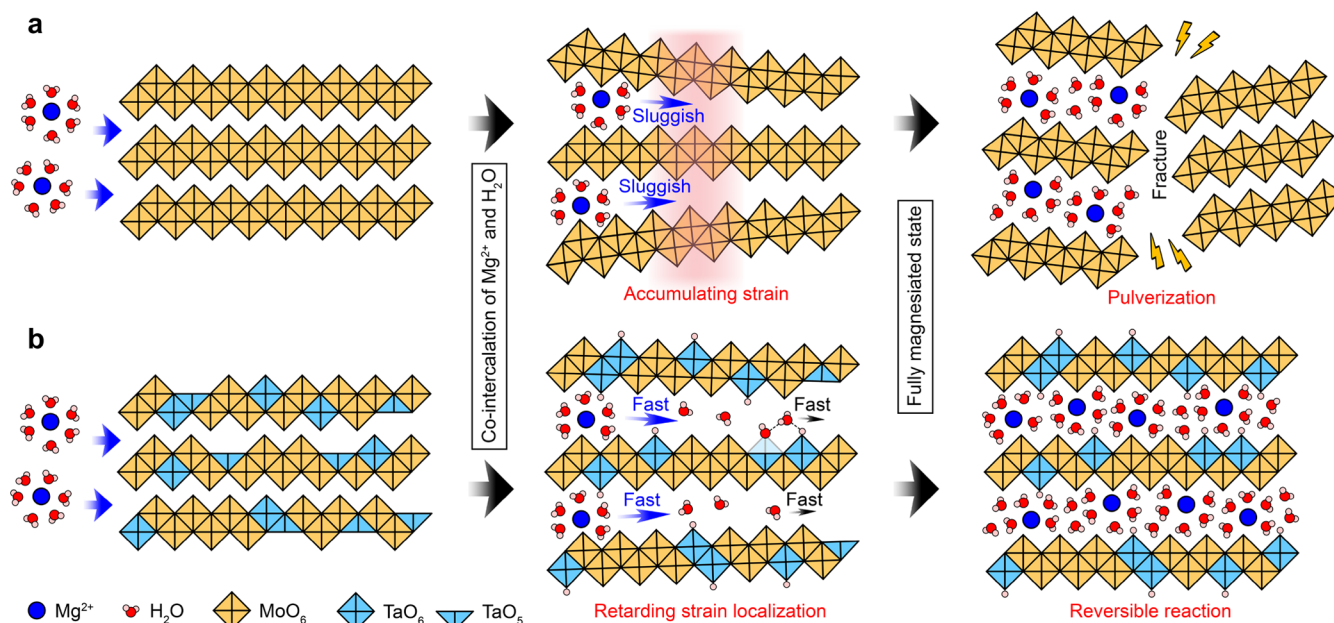
molecule after anchoring to the V_O site in $MoTaO_x$. Hydrogen bonds can facilitate the transfer of $-H$ species, leading to the formation of a terminal $Ta-OH$ configuration. (g) Diffusion of a hydrated Mg^{2+} ion in MoO_3 . The free energy plot is provided as a function of the collective variable defined as the difference between $Mg-O_{(1)}$ and $Mg-O_{(2)}$ distances, where $O_{(1)}$ and $O_{(2)}$ are the O_t atoms binding to Mg^{2+} in the initial and final states, respectively. (h) Diffusion of a hydrated Mg^{2+} ion in $MoTaO_x$. The collective variable is defined the same as that in (g). Color code: Mo, yellow; Ta, azure; O, red; H, white; and Mg, blue.

(de)magnesiated states. In the magnesiated state, the characteristic Mo^{6+} peaks at 236.3 and 233.1 eV split into three doublet peaks at 236.3 eV/233.1 eV, 235.4 eV/232.2 eV, and 234.3 eV/231.2 eV, corresponding to Mo^{6+} , Mo^{5+} , and Mo^{4+} , respectively.^{26,27} During demagnesiation, the intensity of the Mo^{4+} peak decreases, while the Mo^{6+} peak intensity increases, indicating a full reversal of the Mo oxidation state upon demagnesiation, with Mo^{6+} becoming predominant. Notably, no significant changes were observed in the Ta peaks during the magnesiation and demagnesiation processes (Figure S33b), confirming the electrochemical stability of the Ta framework. Additionally, the intensity of the Mg 1s peak reversibly increases and decreases during cycling (Figure S33c), suggesting that the Mo–O bonds serve as active sites for Mg^{2+} intercalation, while the Ta–O bonds maintain the layered structural integrity. In situ Mo K-edge X-ray absorption near-edge structure (XANES) spectroscopy was further employed to investigate the valence state changes within the electrode bulk (Figures 4a and S34).⁴⁵ The absorption edge of $MoTaO_x$ shifted toward the lower-energy region during magnesiation, approaching the edge position of a MoO_2 reference. Conversely, during demagnesiation, the Mo K-edge XANES shifted to a higher-energy region, indicating an increase in the average oxidation state of Mo. The Ta L_3 -edge XANES remained constant throughout the cycling process (Figure 4b), further verifying the electrochemical and structural stability of the Ta–O bonds. Figure 4c displays the corresponding wavelet-transformed EXAFS spectra for Mo and Ta in k -space.^{46,47} In the pristine state, the highest intensity for Mo in k -space occurs at approximately 1.01 \AA^{-1} , attributed to the Mo–O bond.²⁹ During magnesiation, the first-shell peak shifts to higher $R+\Delta R$ and lower k positions, evidencing a lengthening and weakening of the Mo–O bonds. Additionally, the presence of Mo–O–M (where M represents metal cations) resonances at 3.3 \AA^{-1} suggests the formation of Mo–O–Mg resonance. During demagnesiation, the intensity, position, and coordination structure of the Mo–O bonds revert to values similar to those of the pristine state, demonstrating a highly reversible structural evolution. No significant distortion or shift in the Ta–O peaks was observed during cycling, indicating the robust stability of the Ta–O bonds. Variations in the chemical structure during the magnesiation and demagnesiation processes were further examined using *operando* Raman spectroscopy (Figure 4d). Typical Raman bands at 666, 820, and 998 cm^{-1} were identified, corresponding to the O–Mo–O stretching mode ($Mo-O_s$), $Mo=O$ stretching mode ($Mo-O_a$ and $Mo=O_t$) species in $MoTaO_x$, respectively.³³ These characteristic peaks disappear during magnesiation, suggesting that the intercalated hydrated Mg^{2+} ions coordinate with all Mo–O species, forming $Mo-O-Mg \cdot (H_2O)_y$ complexes. This structural change is corroborated by the emergence of a peak at 6.51° in the XRD pattern. During demagnesiation, all Raman peaks intensify and nearly return to their original state, indicating the high reversibility of the structural changes. Notably, the

terminal $Mo=O_t$ species exhibit the most pronounced changes in intensity while consistently maintaining a high relative level during cycling, indicating its role as the dominant sites for Mg^{2+} storage and transport channels.

AIMD simulations were further conducted to elucidate the mechanisms behind the (de)magnesiation processes. As shown in Figure 4e, the intercalated H_2O molecules in the MoO_3 electrode tend to form hydrogen bonds with the O_t atoms, with the OH bonds of H_2O preferentially directed toward the MoO_3 slabs. However, in the $MoTaO_x$ electrode (Figure 4f), the intercalated H_2O molecules anchor firmly to the V_O sites introduced by Ta dopants and rapidly dissociate into $-OH$ and $-H$ species. The $-OH$ species remain at the V_O sites, while the $-H$ species will be transferred through hydrogen bonds to bind with nearby O_t atoms atop Ta atoms. Both species lead to the emergence of a terminal $Ta-OH$ configuration, which could establish hydrogen bonds with the intercalated H_2O molecules in a scenario of $Ta-OH \cdots OH_2$. We note that the dissociation phenomenon is spontaneous in the AIMD simulations at 300 K, meaning that this process is not only exothermic but also exhibits a low kinetic barrier. Therefore, it could be regarded as an additional driving force that favors the intercalation of H_2O molecules before magnesiation of the $MoTaO_x$ electrode, and it could also explain the reason for the incorporation of free H_2O molecules not coordinated with Mg^{2+} .

We further used constrained AIMD simulations via the slow growth method to evaluate the kinetics of Mg^{2+} diffusion in MoO_3 and $MoTaO_x$ electrodes. Due to the formation of hydrogen bonds between H_2O molecules and MoO_3 slabs in the configuration of $Mo-O \cdots H_2O$, the OH bonds in H_2O are weakened, leading to a stronger interaction between the Mg^{2+} ion and its coordinated H_2O molecules (Figure 4g). During the diffusion of Mg^{2+} ions in the MoO_3 electrode, some of the H_2O molecules in their first solvation sheath will depart from them, for which a stronger coordination bond could give rise to a higher kinetic barrier for Mg^{2+} diffusion. Other H_2O molecules tend to accompany the Mg^{2+} ions during their diffusion, with strong coordination bonds resulting in a high steric hindrance between the solvation sheath and its nearby H_2O molecules, which also leads to an increase in the Mg^{2+} diffusion barrier. In contrast, the coordinated H_2O molecules of Mg^{2+} in the $MoTaO_x$ electrode form hydrogen bonds in the configuration of $Ta-OH \cdots OH_2$ (Figure 4h). In this scenario, the coordination bonds around Mg^{2+} are weakened, leading to a much lower kinetic energy barrier during Mg^{2+} diffusion (0.91 eV) as compared to that in MoO_3 (1.95 eV). We note that in MoO_3 , some of the coordination bonds in the Mg^{2+} solvation sheath are much shorter than those in $MoTaO_x$ (~ 1.78 versus $\sim 2.04 \text{ \AA}$, shown in Figure S35), further corroborating the difference in coordination bond strength. Moreover, in the constrained AIMD simulations, the fluctuation of the $Ta-O_t$ bond length is considerably smaller than that of the $Mo-O_t$ bond length (Figure S36), meaning that $Ta-O_t$ bonds are relatively stronger than $Mo-O_t$ and

Scheme 1. Schematic Illustration of (a) MoO_3 and (b) MoTaO_x in (De)magnesiumation Process

therefore the MoTaO_x slabs are more rigid than MoO_3 . This suggests higher structural stability of the former during (de)magnesiumation processes and is in line with the XPS and XAFs data (Figures 4 and S34) showing that terminal Ta–OH functions as a path for Mg^{2+} transport rather than serving as active sites for Mg^{2+} storage.

Overall, we propose the following magnesiumation process for MoO_3 and MoTaO_x electrodes. In MoO_3 (Scheme 1a), Mg^{2+} ions are cointercalated with a considerable amount of H_2O molecules that serve as the solvation sheath of Mg^{2+} . The sluggish diffusion of hydrated Mg^{2+} ions in the magnesiated region leads to a large concentration gradient, with the interlayer distance significantly expanded as compared to that in the nonmagnesiated region. Ascribing to the large mismatch in the interlayer distance, pronounced internal strain is accumulated during the magnesiumation process, which ultimately results in the pulverization of the MoO_3 electrode. In contrast, Ta dopants in the MoTaO_x electrode introduce a non-negligible number of V_O at the O_t sites, which can effectively accommodate the H_2O molecules and induce their dissociation (Scheme 1b). This thermodynamic driving force successfully facilitates the intercalation of H_2O into the MoTaO_x layers prior to magnesiumation, thus reducing the difference in interlayer distance between magnesiated and nonmagnesiated regions. Furthermore, the facile diffusion of hydrated Mg^{2+} ions in MoTaO_x can flatten the concentration landscape, which, along with the more rigid Ta–O bonds, can retard strain localization during the magnesiumation process. Upon Mg^{2+} extraction from the host, H_2O molecules are incorporated to compensate for the volume change, leading to a fluctuation in interlayer distance and lattice distortion of the host, which is evidenced by the disappearance of characteristic XRD peaks (Figure 2b). Conversely, upon Mg^{2+} reintercalation, the electrostatic attraction between Mg^{2+} and the host layers finally results in gradual ordering and contracting.

CONCLUSIONS

In summary, we develop well-defined Ta-doped MoO_3 nanotube arrays to achieve long-lifespan AMIBs. The V_O in

MoTaO_x accommodates and partially dissociates interlayer H_2O to form “Ta–OH...OH₂”, which lowers the migration barriers and accelerates transport of hydrated Mg^{2+} . The fast ion migration flattens interlayer ion-concentration gradients from co-intercalation of Mg^{2+} with excessive H_2O molecules, reduces interlayer spacing mismatch, and thereby delocalizes strain and suppresses pulverization. Consequently, MoTaO_x sustains stable cycling for 75,000 cycles and delivers a cumulative capacity of 7.2 kAh g^{-1} , approximately 7-fold higher than the best prior report. This finding provides valuable insights into the development of new electrode materials that combine long cycle lifespan with high capacity for practical application in AMIBs.

ASSOCIATED CONTENT

Supporting Information

The Supporting Information is available free of charge at <https://pubs.acs.org/doi/10.1021/jacs.5c21656>.

Materials and instrumentation; experimental and theoretical calculation details; SEM; TEM; XPS; XRD; XAS; EQCM; AIMD simulations; extended electrochemical data; etc. (PDF)

AUTHOR INFORMATION

Corresponding Authors

Bowen Jin – State Key Laboratory of Chemical Resource Engineering, Beijing University of Chemical Technology, Beijing 100029, P. R. China; Email: bwjin@buct.edu.cn

Mingfei Shao – State Key Laboratory of Chemical Resource Engineering, Beijing University of Chemical Technology, Beijing 100029, P. R. China; orcid.org/0000-0002-6461-623X; Email: shaomf@mail.buct.edu.cn

Feng Pan – School of Advanced Materials, Peking University, Shenzhen Graduate School, Shenzhen 518055, P. R. China; orcid.org/0000-0002-8216-1339; Email: panfeng@pksuz.edu.cn

Authors

Yu Wu – State Key Laboratory of Chemical Resource Engineering, Beijing University of Chemical Technology, Beijing 100029, P. R. China

Shunning Li – School of Advanced Materials, Peking University, Shenzhen Graduate School, Shenzhen 518055, P. R. China; orcid.org/0000-0002-5381-6025

Yusen Yang – State Key Laboratory of Chemical Resource Engineering, Beijing University of Chemical Technology, Beijing 100029, P. R. China; orcid.org/0000-0003-0624-3241

Jiahui Zeng – School of Advanced Materials, Peking University, Shenzhen Graduate School, Shenzhen 518055, P. R. China

Xue Duan – State Key Laboratory of Chemical Resource Engineering, Beijing University of Chemical Technology, Beijing 100029, P. R. China

Complete contact information is available at:

<https://pubs.acs.org/10.1021/jacs.5c21656>

Author Contributions

[§]Y.W. and S.L. contributed equally to this work. The manuscript was written through contributions of all authors. All authors have given approval to the final version of the manuscript.

Funding

This work was supported by the National Natural Science Foundation of China (22288102, 22090031, 22090030) and the Basic and Applied Basic Research Foundation of Guangdong Province (2023A1515011391).

Notes

The authors declare no competing financial interest.

ACKNOWLEDGMENTS

We acknowledge financial support from the National Natural Science Foundation of China (22288102, 22090031, 22090030) and the Basic and Applied Basic Research Foundation of Guangdong Province (2023A1515011391). We also acknowledge the assistance provided by the beamline at the BSRF (Beijing Synchrotron Radiation Facility) in facilitating our X-ray absorption spectroscopy experiments.

ABBREVIATIONS

AMIBs, aqueous magnesium-ion batteries; MoTaO_x, Ta-doped MoO₃ nanotube array; V_O, oxygen vacancies; O_v, terminal oxygen sites; O_s, symmetric oxygen sites; O_{as}, asymmetric oxygen sites

REFERENCES

- (1) Mao, M. L.; Gao, T.; Hou, S.; Wang, C. S. A critical review of cathodes for rechargeable Mg batteries. *Chem. Soc. Rev.* **2018**, *47*, 8804–8841.
- (2) Guo, L.; Chen, A.; Wang, A.; Hu, Z.; Zhang, H.; Luo, J. Rechargeable Mg–Br₂ battery with ultrafast bromine chemistry. *J. Am. Chem. Soc.* **2024**, *146*, 26855–26862.
- (3) Shin, C.-H.; Lee, H.-Y.; Gyan-Barimah, C.; Yu, J.-H.; Yu, J.-S. Magnesium: Properties and rich chemistry for new material synthesis and energy applications. *Chem. Soc. Rev.* **2023**, *52*, 2145–2192.
- (4) Song, X. M.; Ge, Y.; Xu, H.; Bao, S. S.; Wang, L.; Xue, X. L.; Yu, Q. C.; Xing, Y. Z.; Wu, Z. A.; K, F.; Zhu, T. S.; Zhang, P. B.; Liu, Y. Z.; Wang, Z. J.; Tie, Z. X.; Ma, T.; Jin, Z. Ternary eutectic electrolyte-assisted formation and dynamic breathing effect of the solid-

electrolyte interphase for high-stability aqueous magnesium-ion full batteries. *J. Am. Chem. Soc.* **2024**, *146* (10), 7018–7028.

- (5) Gautam, R. K.; McGrath, J. J.; Wang, X.; Jiang, J. J. Air-stable membrane-free magnesium redox flow batteries. *J. Am. Chem. Soc.* **2024**, *146* (41), 28414–28426.

- (6) Zimmerer, E. K.; Liang, W. T.; Somaskandan, R.; DeToma, E.; Fawcett, C.; Bruck, A. M.; Ma, L.; Ehrlich, S. N.; Zhao, Q.; Gallaway, J. W. Dynamics of Disordered Intermediates During the Two-Electron Alkaline MnO₂ Conversion Reaction for Grid-Scale Batteries. *Joule* **2025**, *9*, No. 102090.

- (7) Zhao, M.; Lv, Y. Q.; Xun, Y. K.; Yang, H. C.; Bo, Z.; Lu, J. Ordered Zinc Electrodeposition from Single-Crystal Units to Polycrystalline Stacking within Solid-Electrolyte Interphase in Battery Anodes. *Nat. Commun.* **2025**, *16*, No. 2843.

- (8) Zhao, M.; Rong, J. F.; Huo, F.; Lv, Y. Q.; Yue, B. W.; Xiao, Y.; Chen, Y.; Hou, G. L.; Qiu, J. S.; Chen, S. M. Semi-Immobilized Ionic Liquid Regulator with Fast Kinetics toward Highly Stable Zinc Anode under – 35 to 60 °C. *Adv. Mater.* **2022**, *34*, No. 2203153.

- (9) Zhong, C.; Deng, Y.; Hu, W.; Qiao, J.; Zhang, L.; Zhang, J. A review of electrolyte materials and compositions for electrochemical supercapacitors. *Chem. Soc. Rev.* **2015**, *44*, 7484–7539.

- (10) Blázquez, J. A.; Maça, R. R.; Leonet, O.; Azaceta, E.; Mukherjee, A.; Zhao-Karger, Z.; Li, Z.; Kovalevsky, A.; Fernández-Barquín, A.; Mainar, A. R.; Jankowski, P.; Rademacher, L.; Dey, S.; Dutton, S. E.; Grey, C. P.; Drews, J.; Häcker, J.; Danner, T.; Latz, A.; Sotta, D.; Palacín, M. R.; Martin, J.; Lastra, J. M. G.; Fichtner, M.; Kundu, S.; Kraysberg, A.; Ein-Eli, Y.; Noked, M.; Aurbach, D. A practical perspective on the potential of rechargeable Mg batteries. *Energy Environ. Sci.* **2023**, *16*, 1964–1981.

- (11) Aurbach, D.; Lu, Z.; Schechter, A.; Gofar, Y.; Gizbar, H.; Turgeman, R.; Cohen, Y.; Moshkovich, M.; Levi, E. Prototype systems for rechargeable magnesium batteries. *Nature* **2000**, *407*, 724–727.

- (12) Li, Z.; Häcker, J.; Fichtner, M.; Zhao-Karger, Z. Cathode materials and chemistries for magnesium batteries: Challenges and opportunities. *Adv. Energy Mater.* **2023**, *13*, No. 2300682.

- (13) Xu, Y.; Deng, X.; Li, Q.; Zhang, G.; Xiong, F.; Tan, S.; Wei, Q.; Lu, J.; Li, J.; An, Q.; Mai, L. Vanadium oxide pillared by interlayer Mg²⁺ ions and water as ultralong-life cathodes for magnesium-ion batteries. *Chem* **2019**, *5*, 1194–1209.

- (14) Ren, Y. L.; Wu, Y.; Wang, Z. L.; Zhang, S. M.; Gao, J. X.; Lu, Y. Q.; Xiao, J.; Han, H. B.; Jin, B. W.; Guo, J.; Shao, M. F. Self-deprotonation of LDHs toward aqueous multi-ion battery cathode. *ACS Sustainable Chem. Eng.* **2025**, *13*, 12669–12679.

- (15) Jin, B. W.; Liu, Y. H.; Cui, J. Y.; Zhang, S. M.; Wu, Y.; Xu, A. N.; Xu, M.; Shao, M. F. Amorphization boost multi-ions storage for high-performance aqueous batteries. *Adv. Funct. Mater.* **2023**, *33*, No. 2301909.

- (16) Hou, S.; Ji, X.; Gaskell, K.; Wang, P.-F.; Wang, L.; Xu, J.; Sun, R.; Borodin, O.; Wang, C. Solvation sheath reorganization enables divalent metal batteries with fast interfacial charge transfer kinetics. *Science* **2021**, *374*, 172–178.

- (17) Li, C.; Shyamsunder, A.; Key, B.; Yu, Z.; Nazar, L. F. Stabilizing magnesium plating by a low-cost inorganic surface membrane for high-voltage and high-power Mg batteries. *Joule* **2023**, *7*, 2798–2813.

- (18) Wang, W. X.; Xiong, F. Y.; Zhu, S. H.; Yan, M. Y.; Liao, X. B.; Yu, K. S.; Cui, L. M.; Chen, J. H.; Wang, J. J.; Lan, R. Q.; Xie, J.; An, Q. Y.; Mai, L. Q. Electron-injection-engineering induced dual-phase MoO_{2.8}F_{0.2}/MoO_{2.4}F_{0.6} heterostructure for magnesium storage. *Natl. Sci. Rev.* **2024**, *11*, No. nwae238.

- (19) Incorvati, J. T.; Wan, L. F.; Key, B.; Zhou, D.; Liao, C.; Fuoco, L.; Holland, M.; Wang, H.; Prendergast, D.; Poepfelmeier, K. R.; Vaughney, J. T. Reversible magnesium intercalation into a layered oxyfluoride cathode. *Chem. Mater.* **2016**, *28*, 17–20.

- (20) Ma, X. F.; Zhao, B. Q.; Liu, H. Y.; Tan, J.; Li, H. Y.; Zhang, X.; Diao, J.; Yue, J. L.; Huang, G. S.; Wang, J. F.; Pan, F. S. H₂O–Mg²⁺ waltz-like shuttle enables high-capacity and ultralong-life magnesium-ion batteries. *Adv. Sci.* **2024**, *11*, No. 2401005.

- (21) He, B.; Ling, Y.; Wang, Z. X.; Gong, W. B.; Wang, Z.; Liu, Y. T.; Zhou, T. Z.; Xiong, T.; Wang, S.; Wang, Y. G.; Li, Q. W.; Zhang, Q. C.; Wei, L. Modulating Selective Interaction of NiOOH with Mg Ions for High-Performance Aqueous Batteries. *eScience* **2024**, *4*, No. 100293.
- (22) Sun, X. Q.; Duffort, V.; Mehdi, B. L.; Browning, N. D.; Nazar, L. F. Investigation of the Mechanism of Mg Insertion in Birnessite in Nonaqueous and Aqueous Rechargeable Mg-Ion Batteries. *Chem. Mater.* **2016**, *28*, 534–542.
- (23) Nam, K. W.; Kim, S.; Lee, S.; Salama, M.; Shterenberg, I.; Gofer, Y.; Kim, J.-S.; Yang, E.; Park, C. S.; Kim, J.-S.; Lee, S.-S.; Chang, W.-S.; Doo, S.-G.; Jo, Y. N.; Jung, Y.; Aurbach, D.; Choi, J. K. The High Performance of Crystal Water Containing Manganese Birnessite Cathodes for Magnesium Batteries. *Nano Lett.* **2015**, *15*, 4071–4079.
- (24) Sun, Y. N.; Ávall, G.; Wu, S. H.; Ferrero, G. A.; Freytag, A.; Groszewicz, P. B.; Wang, H.; Mazzi, K. A.; Bianchini, M.; Baran, V.; Risse, S.; Adelhelm, P. Solvent Co-intercalation in Layered Cathode Active Materials for Sodium-Ion Batteries. *Nat. Mater.* **2025**, *24*, 1441–1449.
- (25) Canepa, P.; Gautam, G. S.; Hannah, D. C.; Malik, R.; Liu, M.; Gallagher, K. G.; Persson, K. A.; Ceder, G. Odyssey of multivalent cathode materials: Open questions and future challenges. *Chem. Rev.* **2017**, *117*, 4287–4341.
- (26) Kim, H.-S.; Cook, J. B.; Lin, H.; Ko, J. S.; Tolbert, S. H.; Ozolins, V.; Dunn, B. Oxygen vacancies enhance pseudocapacitive charge storage properties of MoO_{3-x} . *Nat. Mater.* **2017**, *16*, 454–460.
- (27) Brezesinski, T.; Wang, J.; Tolbert, S. H.; Dunn, B. Ordered mesoporous α - MoO_3 with iso-oriented nanocrystalline walls for thin-film pseudocapacitors. *Nat. Mater.* **2010**, *9*, 146–151.
- (28) Gao, W.; Zhang, Z.; Dou, M.; Wang, F. Highly dispersed and crystalline Ta₂O₅ anchored Pt electrocatalyst with improved activity and durability toward oxygen reduction: Promotion by atomic-scale Pt–Ta₂O₅ interactions. *ACS Catal.* **2019**, *9*, 3278–3288.
- (29) Yang, Y.; Qian, Y.; Li, H.; Zhang, Z.; Mu, Y.; Do, D.; Zhou, B.; Dong, J.; Yan, W.; Qin, Y.; Fang, L.; Feng, R.; Zhou, J.; Zhang, P.; Dong, J.; Yu, G.; Liu, Y.; Zhang, X.; Fan, X. O-coordinated W–Mo dual-atom catalyst for pH-universal electrocatalytic hydrogen evolution. *Sci. Adv.* **2020**, *6*, No. eaba6586.
- (30) Chen, W.; Wang, Y.; Wu, B.; Shi, J.; Li, Y.; Xu, L.; Xie, C.; Zhou, W.; Huang, Y.-C.; Wang, T.; Du, S.; Song, M.; Wang, D.; Chen, C.; Zheng, J.; Liu, J.; Dong, C.-L.; Zou, Y.; Chen, J.; Wang, S. Activated Ni–OH bonds in a catalyst facilitates the nucleophile oxidation reaction. *Adv. Mater.* **2022**, *34*, No. 2105320.
- (31) Chen, W.; Shi, J.; Wu, Y.; Jiang, Y.; Huang, Y.-C.; Zhou, W.; Liu, J.; Dong, C.-L.; Zou, Y.; Wang, S. Vacancy-induced catalytic mechanism for alcohol electrooxidation on nickel-based electrocatalyst. *Angew. Chem. Int. Ed.* **2024**, *63*, No. e202316449.
- (32) Zhang, S.; Zhao, F.; Chen, J.; Fu, J.; Luo, J.; Alahakoon, S. H.; Chang, L.-Y.; Feng, R.; Shakouri, M.; Liang, J.; Zhao, Y.; Li, X.; He, L.; Huan, Y.; et al. A family of oxychloride amorphous solid electrolytes for long-cycling all-solid-state lithium batteries. *Nat. Commun.* **2023**, *14*, No. 3780.
- (33) Ma, H.; Liang, J.; Qiu, J.; Jiang, L.; Ma, L.; Sheng, H.; Shao, M.; Wang, Q.; Li, F.; Fu, Y.; Wang, J.; Xie, E.; Chai, Y.; Lan, W. A biocompatible supercapacitor diode with enhanced rectification capability toward ion/electron-coupling logic operations. *Adv. Mater.* **2023**, *35*, No. 2301218.
- (34) Scatena, L. F.; Brown, M. G.; Richmond, G. L. Water at hydrophobic surfaces: Weak hydrogen bonding and strong orientation effects. *Science* **2001**, *292*, 908–912.
- (35) Lounasvuori, M.; Li Sun, Y. Y.; Mathis, T. S.; Puskar, L.; Schade, U.; Jiang, D. E.; Gogotsi, Y.; Petit, T. Vibrational signature of hydrated protons confined in MXene interlayers. *Nat. Commun.* **2023**, *14*, No. 1322.
- (36) Luo, H. Y.; Ji, X. Y.; Zhang, B. D.; Chen, M.; Wu, X. H.; Zhu, Y. L.; Yu, X. Y.; Wang, J. H.; Zhang, H. T.; Hong, Y. H.; Zou, Y. G.; Feng, G.; Qiao, Y.; Zhou, H. S.; Sun, S. G. Revealing the dynamic evolution of electrolyte configuration on the cathode–electrolyte interface by visualizing (de)solvation processes. *Angew. Chem. Int. Ed.* **2024**, *63*, No. e202412214.
- (37) Wang, Y. H.; Zheng, S. S.; Yang, W. M.; Zhou, R. Y.; He, Q. F.; Radjenovic, P.; Dong, J. C.; Li, S. N.; Zheng, J. X.; Yang, Z. L.; Attard, G.; Pan, F.; Tian, Z. Q.; Li, J. F. In situ Raman spectroscopy reveals the structure and dissociation of interfacial water. *Nature* **2021**, *600*, 81–85.
- (38) Sauerbrey, G. Verwendung von Schwingquarzen zur Wägung dünner Schichten und zur Mikrowägung. *Z. Phys.* **1959**, *155*, 206–222.
- (39) Chu, S. Y.; Zhang, C. C.; Xu, H.; Guo, S. H.; Wang, P.; Zhou, H. S. Pinning effect enhanced structural stability toward a zero-strain layered cathode for sodium-ion batteries. *Angew. Chem. Int. Ed.* **2021**, *60*, 13366–13371.
- (40) Sun, S.; Han, Z.; Liu, W.; Xia, Q. Y.; Xue, L.; Lei, X. C.; Zhai, T.; Su, D.; Xia, H. Lattice pinning in MoO_3 via coherent interface with stabilized Li^+ intercalation. *Nat. Commun.* **2023**, *14*, No. 6662.
- (41) Kundu, D.; Adams, B. D.; Duffort, V.; Vajargah, S. H.; Nazar, L. F. A high-capacity and long-life aqueous rechargeable zinc battery using a metal oxide intercalation cathode. *Nat. Energy* **2016**, *1*, No. 16119.
- (42) Shao, H.; Lin, Z. F.; Xu, K.; Taberna, P.-L.; Simon, P. Electrochemical study of pseudocapacitive behavior of $\text{Ti}_3\text{C}_2\text{T}_x$ MXene material in aqueous electrolytes. *Energy Storage Mater.* **2019**, *18*, 456–461.
- (43) Chien, Y.-C.; Liu, H. D.; Menon, A. S.; Brant, W. R.; Brandell, D.; Lacey, M. J. Rapid determination of solid-state diffusion coefficients in Li-based batteries via intermittent current interruption method. *Nat. Commun.* **2023**, *14*, No. 2289.
- (44) Li, Z. H.; Duan, H. H.; Shao, M. F.; Li, J. B.; O’Hare, D.; Wei, M.; Wang, Z. L. Ordered-vacancy-induced cation intercalation into layered double hydroxides: A general approach for high-performance supercapacitors. *Chem* **2018**, *4*, 2168–2179.
- (45) Ravel, B.; Newville, M. ATHENA, ARTEMIS, HEPHAESTUS: Data analysis for X-ray absorption spectroscopy using IFEFFIT. *J. Synchrotron Radiat.* **2005**, *12*, 537–541.
- (46) Funke, H.; Scheinost, A. C.; Chukalina, M. A new FEFF-based wavelet for EXAFS data analysis. *J. Synchrotron Radiat.* **2007**, *14*, 426–432.
- (47) Funke, H.; Scheinost, A. C.; Chukalina, M. Wavelet analysis of extended X-ray absorption fine structure data. *Phys. Rev. B* **2005**, *71*, No. 094110.